Gold Nanorod Arrays as Plasmonic Cavity Resonators

David P. Lyvers,[†] Jeong-Mi Moon,[†] Alexander V. Kildishev,[‡] Vladimir M. Shalaev,[‡] and Alexander Wei[†,*]

[†]Departments of Chemistry and [‡]Electrical and Computer Engineering, and the Birck Nanotechnology Center, Purdue University, West Lafayette, Indiana 47907

An astonishing variety of optical responses can be generated by the collective excitation of free electrons at metal−dielectric interfaces, better known as surface plasmons.[1,2] For thin Au and Ag films, light can couple strongly with plasmons to produce a characteristic loss of reflectance at a specific angle of incidence, whose sensitivity to changes in surface dielectric provides the basis for biosensors based on surface plasmon resonance (SPR).[1,3] For metal nanoparticles and nanostructured films, interaction with light can result in localized surface plasmon resonances (LSPRs) with wavelength-selective extinction, which is sensitive to surface dielectric as well as particle size and shape.[2,4] Anisotropic particles such as nanorods are especially useful for producing LSPRs with high quality factors and are very sensitive to medium and surface effects, comparable to that of conventional SPR.[5−7]

The plasmonic responses of composite metallodielectric nanomaterials and the dispersion relations which define them are even more intriguing. Periodic metal nanoparticle arrays are known to produce LSPRs, which are often tightly localized between particles, and can be modulated by changes in diameter-spacing ratio and other structural factors.[8,9] Nanoparticle arrays have been employed in SPR[10] and other plasmon-enhanced sensing modalities such as surface-enhanced Raman scattering[11−13] and can also be useful for energy transport[14,15] or as photonic band gaps[16−20] depending on their dimensions. Nanorod arrays have particularly exciting potential in the context of metamaterials: a precise tuning of particle shape and interparticle coupling can

ABSTRACT Hexagonal 2D arrays of Au nanorods support discrete plasmon resonance modes at visible and near-infrared wavelengths when coupled with light at normal incidence (k_z). Reflectance spectra of nanorod arrays mounted on a thin Au baseplate reveal multiple resonant attenuations whose spectral positions vary with nanorod height and the dielectric medium. Simulations using 3D finite-element method calculations reveal harmonic sets of longitudinal standing waves in cavities between nanorods, reminiscent of acoustic waves generated by musical instruments. The nodes and antinodes of these quarter-wave plasmon modes are bounded, respectively, at the base and tips of the array. The number of harmonic resonances and their frequencies can be adjusted as a function of nanorod height, diameter-spacing ratio, and the refractive index of the host medium. Dispersion relations based on these standing-wave modes show strong retardation effects, attributed to the coupling of nanorods *via* transverse modes. Removal of the metal baseplate is predicted to result in resonant transmission through the Au nanorod arrays, at frequencies defined by half-wave modes within the open-ended cavities.

KEYWORDS: nanorods · plasmonics · arrays · nanophotonics · dispersion relation

produce a negative refraction index at visible to near-infrared wavelengths[21] or provide near-field focusing for subwavelength imaging.[22]

Here we present experimental and computational studies on the plasmonic response of two-dimensional (2D) hexagonal arrays of Au nanorods to normal incident light (k_z). Localized plasmon modes are generated as longitudinal standing waves confined between nanorod elements, a fundamentally different response than the interaction of light with individual nanorods[23−26] or the coupling of 2D nanorod arrays with in-plane polarized light ($k_{x,y}$), resulting in plasmonic band gaps.[16−20,27] Reflectance spectra of nanorod arrays on a Au baseplate reveal the existence of multiple harmonics at visible and NIR wavelengths, which can be finely tuned by changes in nanorod height and the dielectric medium. The LSPR modes can be simulated and parametrized by three-dimensional finite-element method (FEM) analysis, enabling the dispersion relation to be correlated with material function.
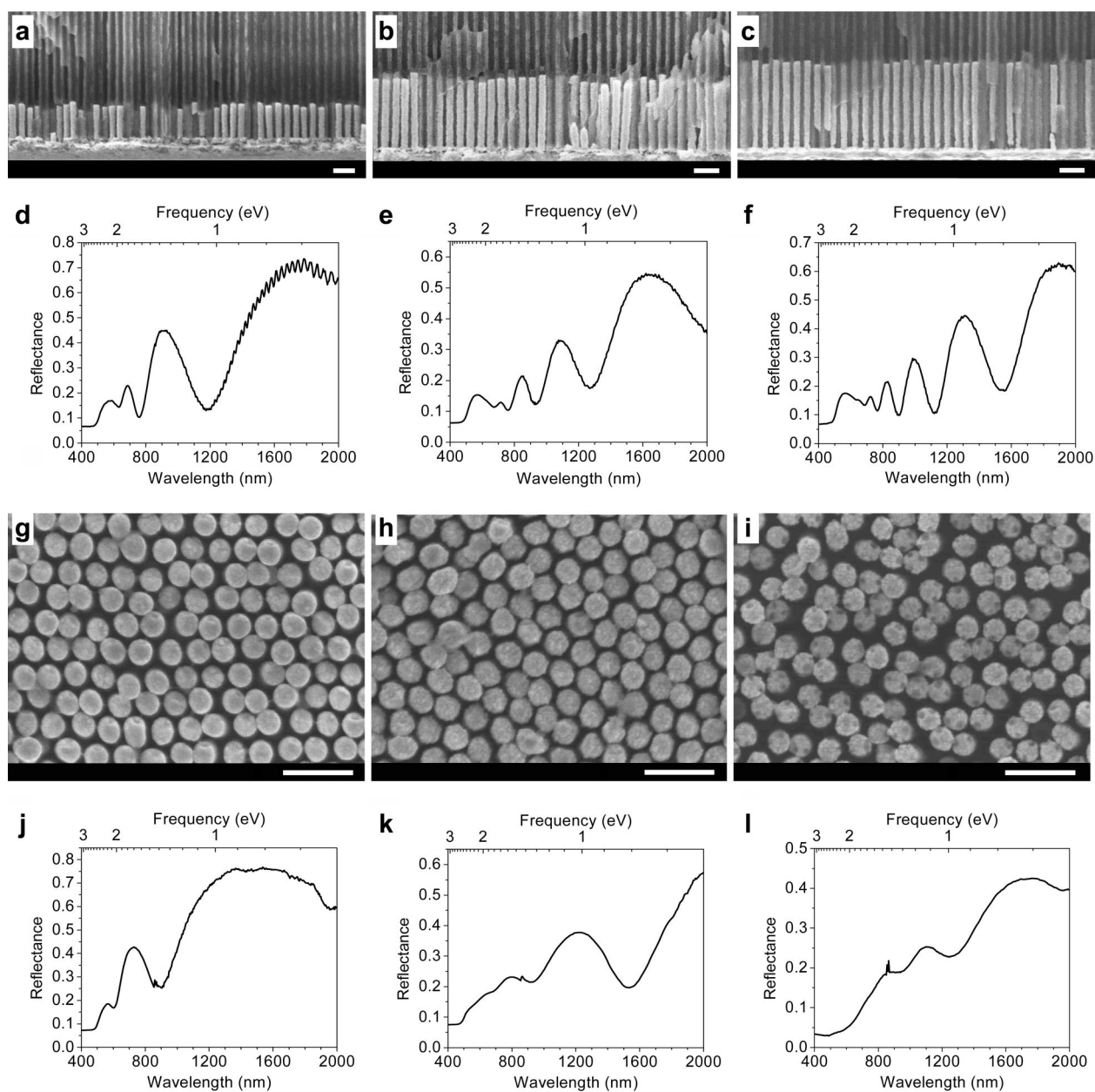
Figure 1. Field-emission scanning electron microscope (FE-SEM) images and vis−NIR reflectance spectra of 2D hexagonal arrays of Au nanorods on metal baseplates. (a−c) Cross-sectional view of Au nanorod arrays in Al_2O_3 membranes (h = 344, 649, and 790 nm; a = 98 nm); (d−f) vis−NIR reflectance spectra of Au nanorod arrays in Al_2O_3 membranes; (g−i) plan view of freestanding Au nanorod arrays (h = 315, 715, and 933 nm; a = 105 nm); (j−l) vis−NIR reflectance spectra of freestanding Au nanorod arrays (in air). Reflectance spectra were acquired with a Lambda 950 spectrophotometer (Perkin-Elmer) using s-polarized light (θ_i = 8°); discontinuity at 850 nm caused by change in photodetector. Scale bar = 250 nm.

RESULTS AND DISCUSSION

Au nanorod arrays of uniform height and aspect ratios (h = 315−933 nm; AR = 3.9−13.3) were prepared as previously described by galvanostatic electrodeposition in nanoporous anodized aluminum oxide (Al_2O_3) templates, conditioned in a 5% polyethyleneimine solution to assist adhesion during Au evaporation and to control the rate of nanorod growth.[28,29] The relative standard deviations in nanorod height in each sample are on the order of 4−7% (Figure 1a−c). The hexagonal 2D arrays are further defined by nanorod diameter (d), periodicity (a), and diameter-spacing ratio $\gamma = d/(a$

− d), all of which are predetermined by their nanoporous templates. Optical reflectance spectroscopy of the Au nanorod arrays supported in Al_2O_3 reveals several pronounced dips or minima at visible and NIR wavelengths (Figure 1d−f). The number of resonant attenuations increases with nanorod height and are accompanied by a pronounced shift toward longer wavelengths. The optical response of the nanorod arrays is superficially similar to the LSPRs described for isolated Au nanorods,[24,30,31] but the plasmon modes involved are very different (see below). It is worth mentioning that earlier optical reflectance studies of colloidal Au in

nanoporous Al_2O_3 membranes were limited to visible wavelengths and could not clearly reveal the resonant attenuations spanning the NIR region.[32,33]

Exposure of the Al_2O_3-supported Au nanorod arrays to aqueous KOH solutions, followed by careful washing and removal of solvent with a critical point dryer, resulted in freestanding Au nanorod arrays with local hexagonal order (Figure 1g–i).[28] These also produce reflectance spectra with resonant attenuations but with fewer modes and at different wavelengths, indicating the critical influence of the dielectric medium on the nanorods' plasmonic response (Figure 1j–l). These minima become less pronounced with increased aspect ratio, an effect attributed to the loss of 2D order due to local aggregation, whereas no such loss in quality factor is observed in the case of membrane-supported Au nanorod arrays. The wavelength-dependent responses of the nanorod 2D arrays to linearly polarized light can be simulated under periodic boundary conditions using FEM analysis. The x,y dimensions of the simulation domain ($a\sqrt{3}/2 \times a/2$), where a is the center-to-center distance between rods, provide the minimal structure required to describe the triangular lattice under periodic boundary conditions, with incident light propagating in the $-z$ direction and polarized along the y axis (Figure 2). The simulation domain contains up to four different regions along the z dimension: (i) above the array ($z > h$), a dielectric region of sufficient thickness ($t > \lambda$) to calculate far-field reflectance with minimal interference from near-field effects; (ii) within the array ($0 < z < h$), the metallodielectric region comprises two quartered Au nanorods embedded in the host medium; (iii) below the array ($z < 0$) the monolithic 50 nm Au baseplate; and (iv) a sublevel vacuum region ($t = 1$ μm) for calculating far-field transmittance. The boundary conditions along the xz and yz planes assume perfect electrically and magnetically conducting walls, respectively, whereas the simulation domain in the z direction is terminated by nonreflecting xy planes.

Introduction of TE-polarized light normal to the array plane ($E_0 = E_y$; $k = -k_z$) produces reflectance spectra with resonant attenuations similar to those observed in the reflectance measurements. Peak matching can be achieved in most cases by adjusting the permittivity of the dielectric medium (Figure 3a–c). For example, an excellent fit is obtained for the resonances produced by Au nanorods in Al_2O_3 membranes with AR = 10.2 and diameter-spacing ratio γ of 1.85 ($h = 649$ nm; $d = 63.6$ nm; $a = 98$ nm) by applying an effective refractive index (n_{eff}) of 1.61, which lies within the range of established values for bulk Al_2O_3 at visible to NIR wavelengths ($n = 1.58–1.62$).[34] Simulated spectra of freestanding Au nanorod arrays in air exhibit fewer resonance peaks as expected; however, peak matching is compromised by the heterogeneous spacing between nanorods in the experimental samples and also
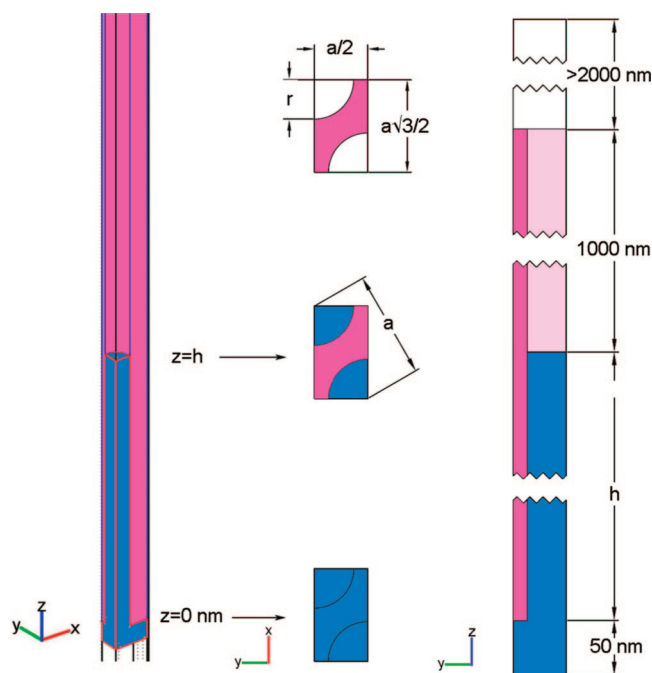

Figure 2. FEM simulation domain for modeling the plasmonic response of Au nanorods in a 2D triangular lattice under periodic boundary conditions. Left, 3D view of simulation domain. Center, x,y cross sections ($a\sqrt{3}/2 \times a/2$; $a = 98$ nm; $d = 72$ nm) of quartered Au nanorods (blue) embedded in a host medium (red); $z = 0$: plane joining Au nanorods and baseplate; $0 < z < h$: Au nanorods embedded in host dielectric; $z > h$: host dielectric and vacuum region without Au nanorods. Right, y,z cross section of simulation domain. Vacuum region below the Au baseplate not shown.

by inhomogeneous peak broadening due to surface roughness or variations in n_{eff} under ambient conditions (Figure 3d–f). In particular, an increase in relative humidity may cause moisture to collect between the freestanding nanorods, which can be compensated for by adjusting n_{eff} to be greater than n_{air}.

The FEM simulations also reveal near-field optical responses associated with the multiple LSPR modes of the Au nanorod arrays (Figure 4). The localized resonances are aptly described as a series of longitudinal standing waves, with an increasing number of harmonics at higher frequencies. The LSPRs are laterally confined between two nanorods and further bounded by a node at the metal baseplate ($z = 0$) and an antinode at the top of the array ($z = h$). The electromagnetic (EM) fields are strongest at the antinodes between the nanorod tips, with enhancements in local field factors $|E_{loc}(\lambda)/E_0(\lambda)|$ of up to an order of magnitude. Localized EM fields between Au nanorods can also be observed under nonresonant (nr) conditions, but the field factors do not exceed the sum of incident and reflected light.

The resonance condition for the coupling of Au nanorod arrays with k_z illumination is akin to the quarter-wave harmonics produced within the acoustic cavities of certain types of musical instruments.[36] Most of the LSPRs confined within the nanorod array exist as higher-order modes; in the example above, the resonance bands at 0.97, 1.35, 1.65, and 1.86 eV (A–D) rep-
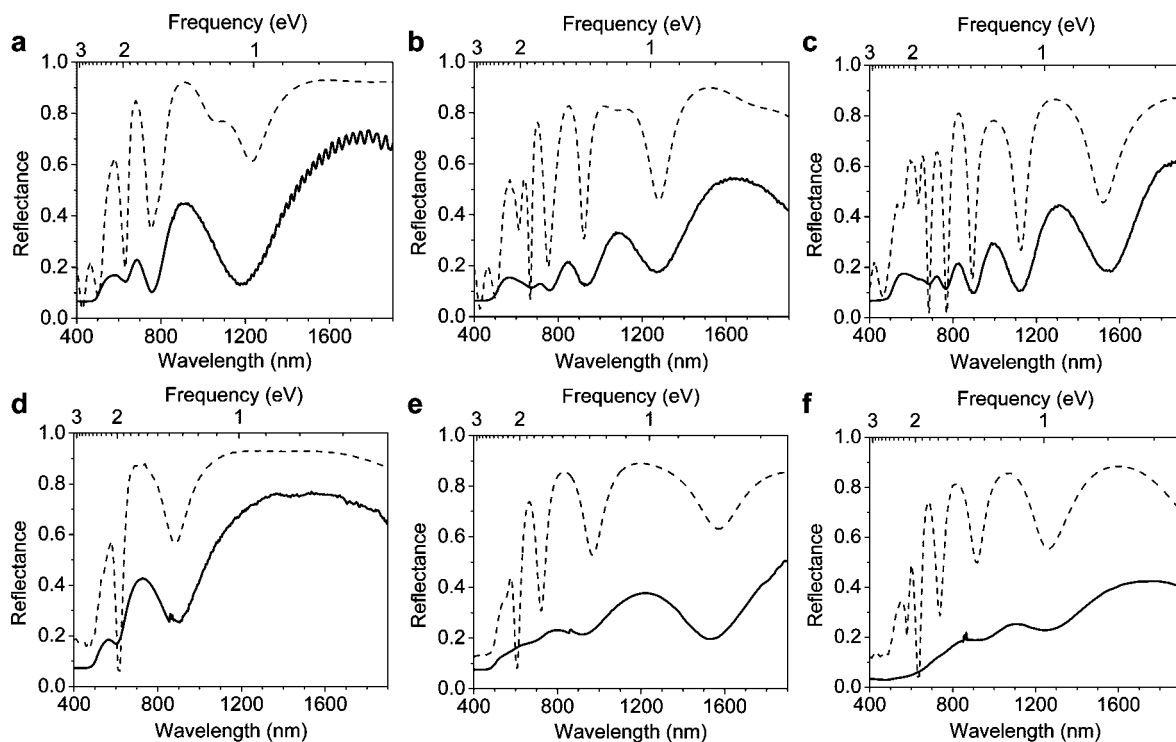
Figure 3. (a−c) Experimental and simulated reflectance spectra of Au nanorod arrays in Al_2O_3 on a 50 nm baseplate. Simulated reflectance spectra ($\lambda = 400−1900$ nm) are normalized by $E(\lambda)$ in the far-field region (at the top of the simulation domain); calculated peak wavelengths are within experimental error of measured values (±2.5 nm). (a) $h = 344$ nm (AR = 5.3; $\gamma = 1.96$; $n_{eff} = 1.625$); (b) $h = 649$ nm (AR = 10.2; $\gamma = 1.85$; $n_{eff} = 1.61$); (c) $h = 790$ nm (AR = 11.0; $\gamma = 2.74$; $n_{eff} = 1.50$). (d−f) Experimental and simulated reflectance spectra of freestanding Au nanorod arrays on a 50 nm baseplate: (d) $h = 315$ nm (AR = 3.9; $\gamma = 2.6$; $n = 1.1$); (e) $h = 715$ nm (AR = 8.8; $\gamma = 3.4$; $n = 1$); (f) $h = 933$ nm (AR = 13.3; $\gamma = 2.0$; $n = 1.07$). For additional parameters affecting relative peak intensities, see Supporting Information (Figure S1).[35]

resent the fifth, seventh, ninth, and 11th harmonic, respectively. However, it should be emphasized that the standing waves within the array are affected by the coupling of *transverse* plasmon modes between nanorods (see below) and are thus distinct from the multipolar LSPRs described for isolated nanorods which require excitation of longitudinal plasmon modes.[23,30,31,37]

A systematic variation of h in the FEM simulations of the Au nanorod arrays reveals the progressive increase in the number of reflectance minima and their resonance wavelengths with aspect ratio (Figure 5). It is interesting to note that the resonance linewidths become narrower as h and AR increase: for example, the fwhm values of the resonances between 0.9 and 1.0 eV ($\lambda = 1250−1400$ nm) decrease from 0.15 eV or 180 nm for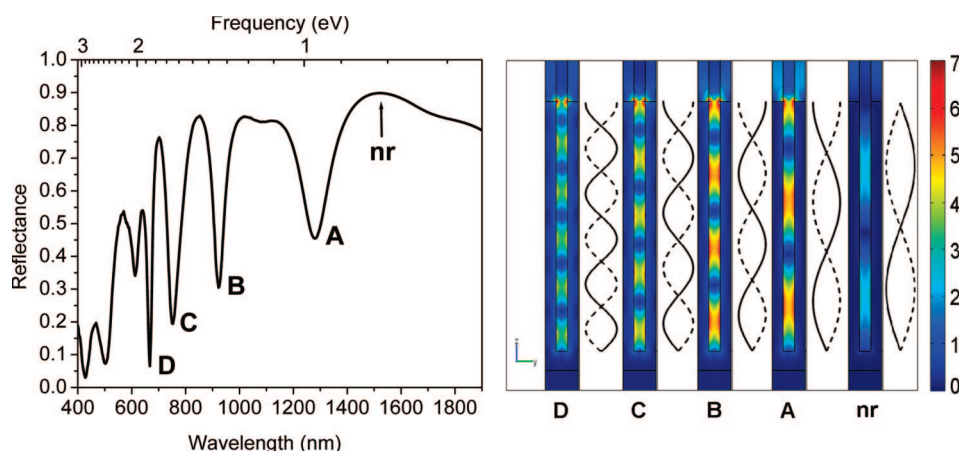 350 nm rod arrays (AR = 4.9) to 0.07 eV or 80 nm for 1150 nm rod arrays (AR = 16.0). This bandwidth reduction can also be observed in the experimental reflectance spectra (Figure 1d−f) and is presumed to be characteristic of the stricter resonance conditions imposed by higher-order modes.

Similar progressions in resonance modes can be generated by increasing n_{eff} (Figure 6). The tunability of these modes with n_{eff} is limited relative to the range of accessible wavelengths by adjustment of nanorod height; nevertheless,

Figure 4. FEM simulations of local electromagnetic fields of 649 nm Au nanorod array in Al_2O_3 (AR = 9.0; $\gamma = 2.77$; $n_{eff} = 1.61$) excited at normal incidence ($E_0 = E_y$). Left, reflectance spectrum with resonance bands A−D ($\lambda = 1280, 922.5, 752.5,$ and 667.5 nm, respectively); right, standing quarter-wave modes A−D confined between nanorods. Local EM fields are strongest near the nanorod tips; EM fields at a nonresonant half-wave mode ($\lambda_{nr} = 1550$ nm) are shown for comparison.
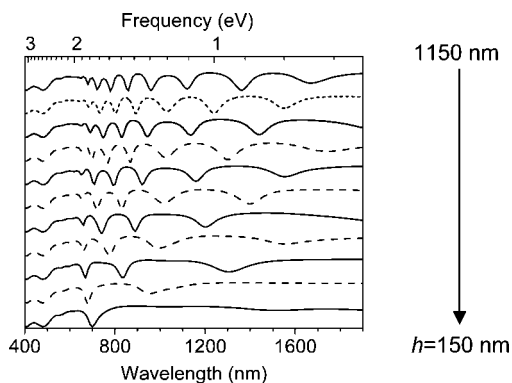
Figure 5. Simulated reflectance spectra (normalized) of Au nanorod arrays in Al$_2$O$_3$ as a function of height (*h*) and aspect ratio (AR) (*d* = 72 nm; γ = 2.77; n_{eff} = 1.61). Δ*h* = 100 nm per plot; see Web-Enhanced Object 1 for semicontinuous variation in *h*.

the resonance peak positions are highly sensitive to their environment and shift by many hundreds of nanometers per refractive index unit (RIU). In the example below, resonance bands A−D experience linear shifts in wavelength with respect to *n* (Δλ/Δ*n* = 767, 636, 456, and 379 nm/RIU, respectively), up to more than twice that reported for isolated plasmon-resonant nanorods.[5−7] The magnitudes of these shifts were confirmed experimentally by collecting reflectance spectra from freestanding Au nanorod arrays immersed in aqueous DMSO mixtures: adjusting the refractive index of the medium from *n* = 1.33 (100% water) to 1.45 (80% DMSO) caused LSPR bands A and B to shift toward longer wavelengths by roughly 850 and 720 nm/ RIU, respectively (Figure 6C and Supporting Information). Discrepancies between the calculated and measured Δλ/Δ*n* may be attributed to limited peak resolution, caused by optical interference by the solvent or loss of periodic order in the nanorod array.

The standing-wave LSPRs are strongly dependent on the coupled transverse modes between closely spaced nanorods but appear to be decoupled from localized

longitudinal modes. Evidence for decoupling comes from reflectance measurements using TE-polarized light at variable angles of incidence ($E_0 = E_y \cos \theta_i + E_z \sin \theta_i$); no significant changes in LSPR peak position or intensity are observed with an increase in θ_i (Figure S3 in Supporting Information). The coupling between transverse modes and its subsequent effect on standing-wave LSPRs can be strengthened by increasing diameter-spacing ratio γ, as demonstrated in FEM calculations of Au nanorod arrays with constant *h* and *a* but variable *d* (Figure 7a). At first glance, the shifts in LSPR peaks with increasing γ appear similar to those observed with increasing *h* or n_{eff} (*cf.* Figure 5), but the local field factors between nanorods also increase with γ due to stronger transverse coupling, intensifying the open-cavity modes (Figure 7b).[9] It is worth noting that the quality of the LSPR modes again increases with *d* and γ. This indicates that the LSPR modes are tightly confined within the interstitial cavities between Au nanorods and are thus relatively free from damping effects typically associated with changes in particle volume.[2]

The standing-wave LSPRs within the 2D nanorod arrays can be used to describe dispersion relations with k_z. For an open cavity of height *h*, the wavevector and its associated harmonics are simply defined as quarter-wave modes:

$$k_i = \frac{(2i+1)\pi}{2h} \tag{1}$$

where 2*i* + 1 is the order of the observed harmonics. The dispersion relation is assumed to be valid for all values of *h* but can vary with respect to other structural parameters such as γ. Input values taken from Figure 5 (*d* = 72 nm, γ = 2.77, n_{eff} = 1.61) indicate that the plasmon frequencies within Al$_2$O$_3$-supported Au nanorod arrays are significantly retarded when compared with propagating plasmon modes at a smooth Au−Al$_2$O$_3$ in-
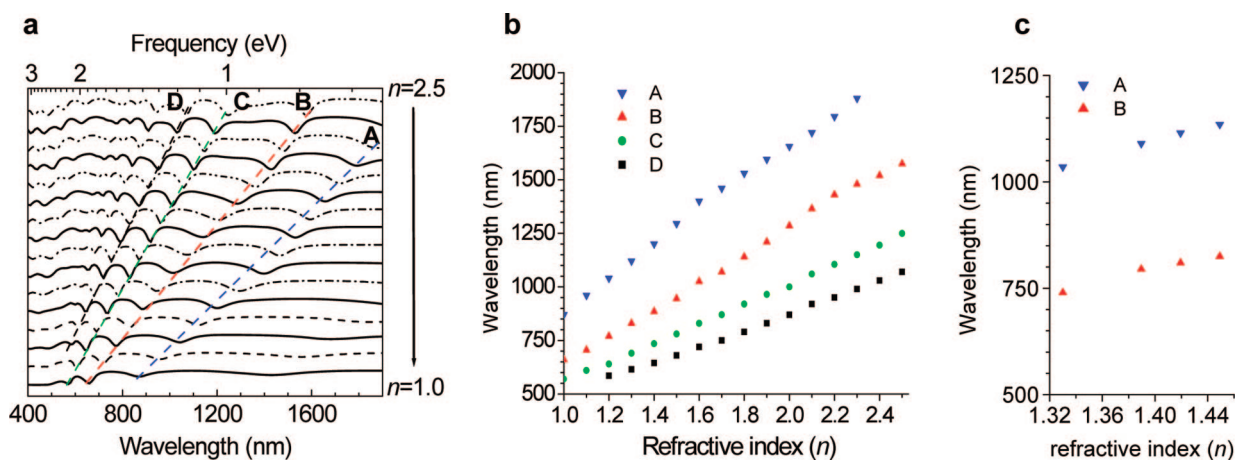

Figure 6. Standing-wave LSPRs of Au nanorod arrays in Al$_2$O$_3$ as a function of refractive index (n_{eff}) (*h* = 649 nm; AR = 9.0; γ = 2.77). (a) Simulated reflectance spectra illustrating red shifts for higher-order resonance bands A−D; (b) LSPR wavelengths plotted as a function of *n*, with Δλ/Δ*n* as high as 767 nm/RIU; (c) experimental Δλ/Δ*n* measurements using freestanding Au nanorod arrays immersed in aqueous DMSO mixtures. See Web-Enhanced Object 2 for semicontinuous variation in n_{eff}.
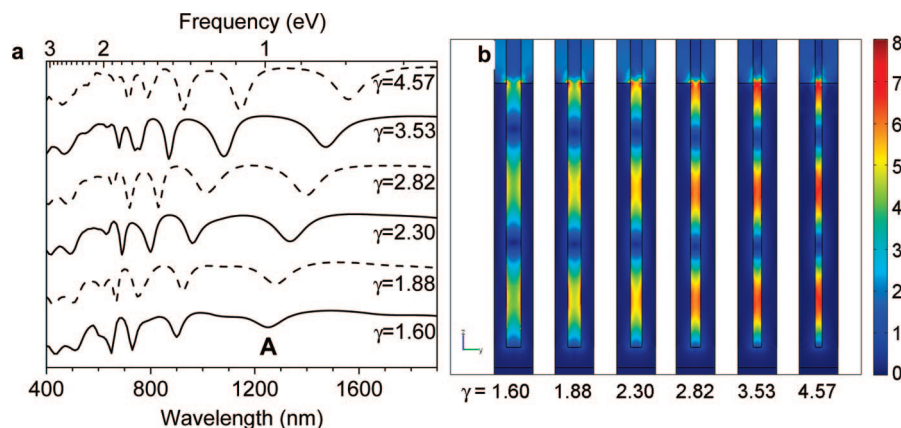
Figure 7. (a) Simulated reflectance spectra of Au nanorod arrays as a function of diameter-spacing ratio (γ). Nanorod height, periodicity, and refractive index are held constant ($h = 649$ nm; $a = 98$ nm; $n_{eff} = 1.61$). (b) Local EM fields associated with standing-wave cavity mode A; field factors intensify as γ increases from 1.60 to 4.57.
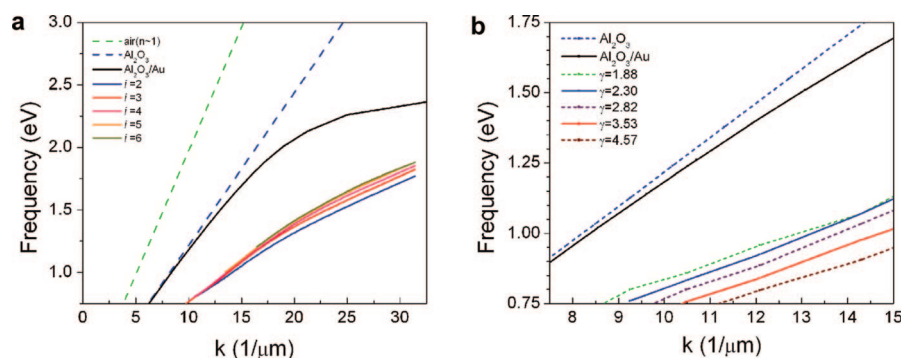

Figure 8. (a) Dispersion relation for standing-wave modes ($i = 2-5$) of Au nanorod arrays in Al_2O_3 ($d = 72$ nm, $\gamma = 2.77$, $n_{eff} = 1.61$; cf. Figure 5), compared with light line in Al_2O_3 (dark blue, dashed) and for SPP modes at a planar Au/Al_2O_3 interface (black). (b) Dispersion relations ($i = 2$) of Au nanorod arrays in Al_2O_3 with variable γ ($a = 98$ nm, $n_{eff} = 1.61$; cf. Figure 7).
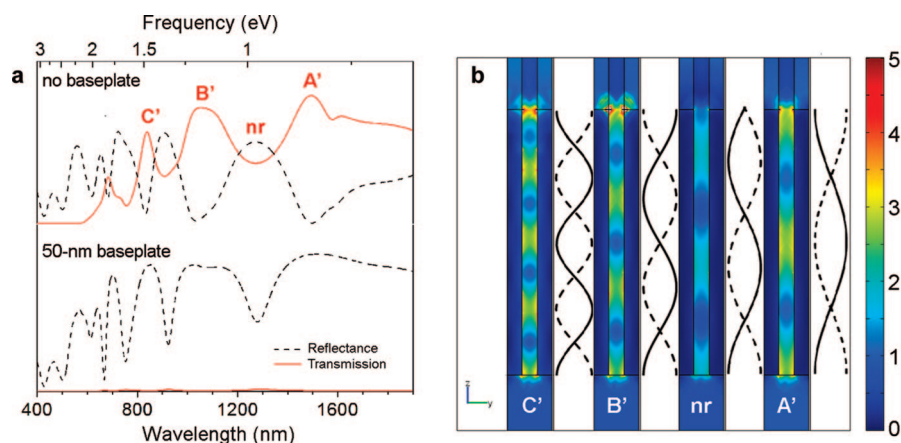

Figure 9. (a) Top: Simulated transmission and reflectance spectra of Au nanorod arrays supported in Al_2O_3 with no reflective baseplate: $h = 649$ nm; AR = 10.2; $\gamma = 1.85$; $n_{eff} = 1.61$; transmission bands A′−C′ exist as half-wave cavity modes centered at 0.83, 1.20, and 1.49 eV, respectively. Bottom: Reflectance spectra of Au nanorod arrays in Al_2O_3 with Au baseplate, shown for comparison; transmission is negligible. (b) Local EM fields of half-wave modes A′−C′ and at an off-resonance (quarter-wave) stop band (nr, 0.98 eV).

6a). Further retardation is observed with an increase in diameter-spacing ratio γ (Figure 8b), in accord with the previously discussed role of coupled transverse modes on plasmon confinement. The strong retardation effect of the hexagonal Au nanorod arrays on k_z is a significant departure from an earlier study on the interaction of in-plane light with Au nanorod "half-wave antennae" on quartz, whose dispersion relation was found to be quite similar to that of a continuous Au/SiO_2 interface.[24]

FEM analysis also suggests that the supported Au nanorod arrays may be converted from optical cavity resonators into resonant transmission filters, whose propagation modes can be defined by a similar dispersion relation. Far-field transmission through nanorod arrays on 50 nm Au baseplates was found to be negligible by both experiment and simulation, although the latter indicates nonzero transmission at LSPR frequencies and suggests its possible detection by near-field methods. Removing the metal baseplate creates open channels between nanorods, with resonance conditions defined by antinodes at the top and bottom of the array. These modes are expected to exist as half-wave harmonics; transmission bands associated with the second, third, and fourth harmonic frequencies (A′−C′) are shown (Figure 9). The LSPR modes previously associated with resonant attenuations are now out of phase by 90° and replaced with nonresonant stop bands. These simulations show that the function and resonance modes of the nanorod arrays change completely upon decoupling from a reflective substrate.

The identification of standing-wave modes within hexagonal 2D arrays of plasmon-resonant nanorods gives rise to several interesting opportunities for nanophotonics. One possibility is to combine nanorod arrays with surface-emitting lasing materials to enhance optical gain, as recently demonstrated with nanoparticle dimers.[38,39] The nanosized cavities can also be engi-

terface (Figure 8a). The dispersion relations also vary modestly with respect to i and reflect the greater sensitivity of lower-order harmonic modes to changes in array height and the dielectric medium (cf. Figures 5 and

neered to enhance multiple resonance modes in the NIR to support a variety of nonlinear optical effects. Hexagonal 2D arrays of Ag nanorods can be expected to produce very similar effects, with the added benefit of higher-quality resonances at visible frequencies.[40] Finally, the dielectric matrix itself can be modified to provide complementary material function that can exploit the resident field factors within the resonant cavities.

METHODS

Templated Synthesis of Hexagonal 2D Arrays of Au Nanorods. Nanoporous Al_2O_3 templates were prepared by a two-step anodization process reported by Masuda and co-workers.[41,42] Strips of high-grade Al foil (Sigma-Aldrich, 99.999%, $50 \times 10 \times 0.25$ mm) were sonicated for 1 h in trichloroethylene, followed by electropolishing in 70% perchloric acid (70 mL) and ethanol (350 mL) for 5 min at 10 °C at 14.5 V using a dc power supply (Sorensen DCR 20-40A) and a Pt wire mesh as the cathode. All samples where rinsed thoroughly with deionized water before and after each step. The electropolished Al foil was anodized for $18-24$ h in 0.3 M oxalic acid solution at 5 °C at a constant voltage of 40 V with a graphite plate (5×2 cm) as the cathode. The Al_2O_3 was removed using an etching solution of phosphoric acid (6% w/v) and chromic acid (1.6% w/v) for 4 h at 60 °C. A second anodization was carried out for $7-10$ h as described above, followed by dissolution of the underlying Al substrate in saturated $HgCl_2$ to yield nanoporous Al_2O_3 templates with thicknesses of $30-40$ μm. Subsequent exposure to 0.1 M phosphoric acid for 1 h at 30 °C yielded hexagonally ordered pores with periodicities (a) of $95-105$ nm and mean diameters (d) of $60-75$ nm. The nanoporous templates were then soaked in a 5% polyethyleneimine solution ($M_w = 25\,000$) for 5 h at room temperature, followed immediately by multiple washes in deionized water (6×10 min). The templates were dried in a vacuum oven for a minimum of 8 h at 100 °C then coated with a 50 nm layer of Au by thermal evaporation.

Electrodepositions were performed at ambient temperature under galvanostatic conditions using a commercial Au plating solution (Orotemp 24, Technic Inc.), with a Pt wire counter electrode and a saturated calomel electrode (SCE) as a reference. The Au-backed templates were placed in a homemade Teflon electrochemical cell as previously described.[28] Nanorods were grown at a constant current density of 1.26 mA/cm^2 and observed to be approximately linear with respect to the delivered charge. All nanorod arrays were characterized by FE-SEM (Hitachi S-4800), followed by image size analysis using a commercial software package (SigmaScan Pro 5).

Optical Reflectance Measurements. Reflectance measurements were performed on a visible−NIR optical measurement system (Perkin-Elmer Lambda 950) with a fixed-angle reflector (8°) and calibrated against a diffuse reflectance standard (Spectralon SRM-99). Specular reflectances were generated using either s- or p-polarized light and a spot size commensurate with the size of the nanorod array (*ca.* 5 mm) and dispersed within a 150 mm diffuse integrating sphere. Optical measurements of Au nanorods on 50 nm metal baseplates performed in transmission mode did not produce detectable signal.

Finite Element Method Analysis. The wavelength-dependent response of the nanorod arrays to linearly polarized light at normal incidence was simulated under periodic boundary conditions using a commercial full-wave 3D FEM package with an adaptive meshing routine (COMSOL Multiphysics with RF module). The simulation domain comprises four distinct geometries: the Au nanorod array (2 quarter rods plus baseplate), the porous host medium (typically Al_2O_3, $n = 1.61$), and two vacuum regions ($n = 1$) above and below the array with sufficient thickness for simulating far-field reflectance and transmission, respectively. Complex dielectric values for Au nanorods were interpolated from bulk optical constants reported by Johnson and Christy.[43] FEM simulations of the harmonic propagation of electromagnetic waves were performed on a PC workstation with the assumed absence of free charges and were found to be sufficient for matching with experimental measurements. Reflectance spectra were produced according to eq 2:

$$R = \left(\frac{E_{tot} - E_i}{E_i}\right)^2 \qquad (2)$$

where E_{tot} and E_i represent the intensities of the total and incident electric fields, respectively.

Supporting Information Available: Description of loss factor for adjusting relative intensity of LSPR modes (Figure S1); reflectance spectra of freestanding Au nanorod arrays as a function of solvent dielectric (Figure S2); reflectance spectra of Al_2O_3-supported Au nanorod arrays as a function of incident angle (Figure S3). This material is available free of charge *via* the Internet at http://pubs.acs.org.

REFERENCES AND NOTES

1. Raether, H. *Surface Plasmons on Smooth and Rough Surfaces and on Gratings*; Springer-Verlag: Berlin, 1988.
2. Kreibig, U.; Vollmer, M. *Optical Properties of Metal Clusters*; Springer: New York, 1995.
3. Homola, J. Present and Future of Surface Plasmon Resonance Biosensors. *Anal. Bioanal. Chem.* **2003**, *377*, 528–539.
4. Wei, A. In *Nanoparticles: Scaffolds and Building Blocks*; Rotello, V. M., Ed.; Kluwer Academic: New York, 2004; pp 173−200.
5. McFarland, A. D.; van Duyne, R. P. Single Silver Nanoparticles as Real-Time Optical Sensors With Zeptomole Sensitivity. *Nano Lett.* **2003**, *3*, 1057–1062.
6. Yu, C. X.; Irudayaraj, J. Multiplex Biosensor Using Gold Nanorods. *Anal. Chem.* **2007**, *79*, 572–579.
7. Hansen, M. N.; Chang, L.-S.; Wei, A. Resorcinarene-Encapsulated Gold Nanorods: Solvatochromatism and Magnetic Nanoshell Formation. *Supramol. Chem.* **2008**, *20*, 35–40.
8. Kim, B.; Tripp, S. L.; Wei, A. Self-Organization of Large Gold Nanoparticle Arrays. *J. Am. Chem. Soc.* **2001**, *123*, 7955–7956.
9. Genov, D. A.; Sarychev, A. K.; Shalaev, V. M.; Wei, A. Resonant Field Enhancements from Metal Nanoparticle Arrays. *Nano Lett.* **2004**, *4*, 153–158.
10. Lyon, L. A.; Pena, D. J.; Natan, M. J. Surface Plasmon Resonance of Au Colloid-Modified Au Films: Particle Size Dependence. *J. Phys. Chem. B* **1999**, *103*, 5826–5831.
11. Wei, A.; Kim, B.; Sadtler, B.; Tripp, S. L. Tunable Surface-Enhanced Raman Scattering from Large Gold Nanoparticle Arrays. *ChemPhysChem* **2001**, *2*, 743–745.
12. Wang, H.; Levin, C. S.; Halas, N. J. Nanosphere Arrays with Controlled Sub-10-nm Gaps as Surface-Enhanced Raman Spectroscopy Substrates. *J. Am. Chem. Soc.* **2005**, *127*, 14992–14993.
13. Wang, H.-H.; Liu, C.-Y.; Wu, S.-B.; Liu, N.-W.; Peng, C.-Y.; Chan, T.-H.; Hsu, C.-F.; Wang, J.-K.; Wang, Y.-L. Highly Raman-Enhancing Substrates Based on Silver Nanoparticle Arrays with Tunable Sub-10 nm Gaps. *Adv. Mater.* **2006**, *18*, 491–495.

14. Maier, S. A.; Brongersma, M. L.; Kik, P. G.; Atwater, H. A. Observation of Near-Field Coupling in Metal Nanoparticle Chains using Far-Field Polarization Spectroscopy. *Phys. Rev. B* **2002**, *65*, 193408-1–193408-4.

15. Maier, S. A.; Kik, P. G.; Atwater, H. A.; Meltzer, S.; Harel, E.; Koel, B. E.; Requicha, A. A. G. Local Detection of Electromagnetic Energy Transport below the Diffraction Limit in Metal Nanoparticle Plasmon Waveguides. *Nat. Mater.* **2003**, *2*, 229–232.

16. Moroz, A. Three-Dimensional Complete Photonic Band-Gap Structures in the Visible. *Phys. Rev. Lett.* **1999**, *83*, 5274–5277.

17. van der Lem, H.; Moroz, A. Towards Two-Dimensional Complete Photonic-Bandgap Structures below Infrared Wavelengths. *J. Opt. A: Pure Appl. Opt.* **2000**, *2*, 395–399.

18. Zhang, W. Y.; Lei, X. Y.; Wang, Z. L.; Zheng, D. G.; Tam, W. Y.; Chan, C. T.; Sheng, P. Robust Photonic Band Gap from Tunable Scatterers. *Phys. Rev. Lett.* **2000**, *84*, 2853–2856.

19. Wang, Z.; Chan, C. T.; Zhang, W.; Ming, N.; Sheng, P. Three-Dimensional Self-Assembly of Metal Nanoparticles: Possible Photonic Crystal with a Complete Gap below the Plasma Frequency. *Phys. Rev. B* **2001**, *64*, 113108-1–113108-4.

20. Veronis, G.; Dutton, R. W.; Fan, S. Metallic Photonic Crystals with Strong Broadband Absorption at Optical Frequencies over Wide Angular Range. *J. Appl. Phys.* **2005**, *97*, 093104-1–093104-4.

21. Shalaev, V. M.; Cai, W. S.; Chettiar, U. K.; Yuan, H. K.; Sarychev, A. K.; Drachev, V. P.; Kildishev, A. K. Negative Index of Refraction in Optical Metamaterials. *Opt. Lett.* **2005**, *30*, 3356–3358.

22. Ono, A.; Kato, J.; Kawata, S. Subwavelength Optical Imaging Through a Metallic Nanorod Array. *Phys. Rev. Lett.* **2005**, *95*, 267407-1–267407-4.

23. Krenn, J. R.; Schider, G.; Rechberger, W.; Lamprecht, B.; Leitner, A.; Aussenegg, F. R. Design of Multipolar Plasmon Excitations in Silver Nanoparticles. *Appl. Phys. Lett.* **2000**, *77*, 3379–3381.

24. Schider, G.; Krenn, J. R.; Hohenau, A.; Ditlbacher, H.; Leitner, A.; Aussenegg, F. R.; Schaich, W. L.; Puscasu, I.; Monacelli, B.; Boreman, G. Plasmon Dispersion Relation of Au and Ag Nanowires. *Phys. Rev. B* **2003**, *68*, 155427-1–155427-4.

25. Félidj, N.; Laurent, G.; Aubard, J.; Lévi, G.; Hohenau, A.; Krenn, J. R.; Aussenegg, F. R. Grating-Induced Plasmon Mode in Gold Nanoparticle Arrays. *J. Chem. Phys.* **2005**, *123*, 221103-1–221103-5.

26. Evans, P.; Wurtz, G. A.; Atkinson, R.; Hendren, W. R.; O'Connor, D.; Dickson, W.; Pollard, R. J.; Zayats, A. V. Plasmonic Core/Shell Nanorod Arrays: Subattoliter Controlled Geometry and Tunable Optical Properties. *J. Phys. Chem. C* **2007**, *111*, 12522–12527.

27. Rahachou, A. I.; Zozoulenko, I. V. Light Propagation in Nanorod Arrays. *J. Opt. A: Pure Appl. Opt.* **2007**, *9*, 265–270.

28. Moon, J.-M.; Wei, A. Uniform Gold Nanorod Arrays from Polyethylenimine-Coated Alumina Templates. *J. Phys. Chem. B* **2005**, *109*, 23336–23341.

29. Moon, J.-M.; Wei, A. Controlled Growth of Gold Nanorod Arrays from Polyethylenimine-Coated Alumina Templates. *Mater. Res. Soc. Symp. Proc.* **2006**, *900E*, O.12.32-112.32-7.

30. Payne, E. K.; Shuford, K. L.; Park, S.; Schatz, G. C.; Mirkin, C. A. Multipole Plasmon Resonances in Gold Nanorods. *J. Phys. Chem. B* **2006**, *110*, 2150–2154.

31. Khlebtsov, B. N.; Khlebtsov, N. G. Multipole Plasmons in Metal Nanorods: Scaling Properties and Dependence on Particle Size, Shape, Orientation, and Dielectric Environment. *J. Phys. Chem. C* **2007**, *111*, 11516–11527.

32. Goad, D. G. W.; Moskovits, M. Colloidal Metal in Aluminum-Oxide. *J. Appl. Phys.* **1978**, *49*, 2929–2934.

33. McMillan, B. G.; Berlouis, L. E. A.; Cruickshank, F. R.; Pugh, D. Transverse and Longitudinal Surface Plasmon Resonances of a Hexagonal Array of Gold Nanorods Embedded in an Alumina Matrix. *Appl. Phys. Lett.* **2005**, *86*, 211912-1–211912-3.

34. Eriksson, T. S.; Hjortsberg, A.; Niklasson, G. A.; Granqvist, C. G. Infrared Optical Properties of Evaporated Alumina Films. *Appl. Opt.* **1981**, *20*, 2742–2746.

35. Drachev, V. P.; Chettiar, U. K.; Kildishev, A. V.; Yuan, H.-K.; Cai, W.; Shalaev, V. M. The Ag Dielectric Function in Plasmonic Metamaterials. *Opt. Express* **2008**, *16*, 1186–1195.

36. Fletcher, N. H.; Rossing, T. D. *The Physics of Musical Instruments*; Springer-Verlag: New York, 1991.

37. Encina, E. R.; Coronado, E. A. Resonance Conditions for Multipole Plasmon Excitation in Noble Netal Nanorods. *J. Phys. Chem. C* **2007**, *111*, 16796–16801.

38. Cubukcu, E.; Kort, E. A.; Crozier, K. B.; Capasso, F. Plasmonic Laser Antenna. *Appl. Phys. Lett.* **2006**, *89*, 093120.

39. Yu, N.; Cubukcu, E.; Diehl, L.; Bour, D.; Corzine, S.; Zhu, J.; Kort, E. A.; Hofler, G.; Crozier, K. B.; Capasso, F. Bowtie Plasmonic Quantum Cascade Laser Antenna. *Opt. Express* **2007**, *15*, 13272–13281.

40. Evans, P. R.; Kullock, R.; Hendren, W. R.; Atkinson, R.; Pollard, R. J.; Eng, L. M. Optical Transmission Properties and Electric Field Distribution of Interacting 2D Silver Nanorod Arrays. *Adv. Funct. Mater.* **2008**, *18*, 1075–1079.

41. Masuda, H.; Fukuda, K. Ordered Metal Nanohole Arrays Made by a Two-Step Replication of Honeycomb Structures of Anodic Alumina. *Science* **1995**, *268*, 1466–1468.

42. Masuda, H.; Satoh, M. Highly Ordered Nanochannel-Array Architecture in Anodic Alumina. *Jpn. J. Appl. Phys., Part 2* **1996**, *35*, L126–L129.

43. Johnson, P. B.; Christy, R. W. Optical Constants of the Noble Metals. *Phys. Rev. B* **1972**, *6*, 4370–4379.